PHYSICAL REVIEW A **109**, 043107 (2024)

# Ultrafast formation dynamics of $D_3^+$ from bimolecular reaction of the $D_2$-$D_2$ dimer

Hao Huang,[1] Haomai Hou,[1] Jin Wen,[2,*] Hongcheng Ni,[1,3,†] and Jian Wu[1,3,‡]

[1]*State Key Laboratory of Precision Spectroscopy, East China Normal University, Shanghai 200241, China*
[2]*State Key Laboratory for Modification of Chemical Fibers and Polymer Materials, College of Materials Science and Engineering, Donghua University, Shanghai 201620, China*
[3]*Collaborative Innovation Center of Extreme Optics, Shanxi University, Taiyuan, Shanxi 030006, China*

(Received 2 November 2023; revised 4 March 2024; accepted 19 March 2024; published 5 April 2024)

Bimolecular reactions involving small diatomic molecules constitute a fundamental category of chemical processes. Recent experimental breakthroughs have enabled precise timing of the ultrafast formation dynamics of $D_3^+$ originating from the $D_2$-$D_2$ dimer. In this paper, we systematically survey diverse theoretical approaches for numerically simulating bimolecular reaction dynamics, considering various initial geometric configurations of the dimer. Our findings demonstrate the consistency and reliability of both classical and quantum methods in predicting the reaction timescale for $D_3^+$ formation. Additionally, we illustrate the intricate microscopic details of bimolecular reactions, laying the foundation for comprehending intermolecular interactions.

DOI: 10.1103/PhysRevA.109.043107

## I. INTRODUCTION

Bimolecular reactions represent a class of fundamental processes in chemistry, encapsulating intricate molecular dynamics phenomena. Among these, the formation of the trihydrogen cation $H_3^+/D_3^+$ from the hydrogen dimer $H_2$-$H_2$/$D_2$-$D_2$ represents a basic while pivotal instance. The significance of this reaction extends beyond its unique bonding properties and versatility. As a proton donor, the resulting $H_3^+$ serves as the initiator for the majority of chemical reactions within interstellar clouds, a phenomenon that has attracted substantial attention in the past two decades [1–12]. Previous investigations have revealed the origin of trihydrogen cation formation within interstellar molecular clouds, attributing it to the cosmic-ray ionization of hydrogen molecules [13]. The subsequent reaction ($H_2 + H_2^+ \rightarrow H_3^+ + H$) is widely regarded as the principal pathway leading to $H_3^+$ formation, with extensive experimental research elucidating kinetic energy and angular distribution of products, reaction rate coefficients, and state-selective cross sections [14–16].

Recent experimental advances have allowed for precise temporal characterization of the formation dynamics of trihydrogen cations, pinpointing a reaction timescale on the order of hundreds of femtoseconds [17,18]. This achievement was facilitated by starting from the initial configuration of a dimer state, providing a known initial separation and, consequently, a well-defined spatial starting point. The temporal starting point, essential for timing the bimolecular reaction, was enabled by employing a femtosecond pump-probe setup. Notably, these studies employed classical trajectories to describe nuclear motion, similar to the approach used in most prior molecular dynamics calculations. A crucial question thus remains unanswered: does the timescale for ultrafast formation dynamics differ when accounting for the quantum nature of the bimolecular reaction?

Chemical reactions inherently involve the cleavage and formation of chemical bonds. In systems with a high degree of freedom, the reaction dynamics can become intricate, often obscuring the underlying physical processes. In such scenarios, one would typically focus on the principal coordinates relevant to the reaction, often termed the reaction coordinates, which clarify and simplify the understanding and tracking of reaction dynamics. After defining these reaction coordinates, potential energy surfaces can be constructed through first-principle quantum chemical calculations. Subsequent nuclear dynamical evolution occurs on these potential energy surfaces and can be examined using various theoretical methods. In addition to employing classical trajectories, the nuclear wave packet can be propagated on the potential energy surface (PES) by numerically solving the time-dependent Schrödinger equation (TDSE), offering a quantum perspective on reaction dynamics. Effective information contained within the time-dependent nuclear wave packet can be extracted using approaches such as the virtual detector method [19–22], Bohmian mechanics (BM) [23–30], and backpropagation (BP) [31–34].

In this article, we focus on the elementary ultrafast reaction dynamics of $D_3^+$ formation from the $D_2$-$D_2$ dimer, aiming to explore nuclear motion from both quantum and classical perspectives. We systematically compare different theoretical methods for achieving time resolution in ultrafast bimolecular reaction dynamics. Our results reveal that, when properly implemented, these methods yield similar timescales for the chemical reaction, thus affirming their reliability. It also demonstrates the limited influence of quantum effects on nuclear motion. In addition, we systematically explore the

---

[*] jinwen@dhu.edu.cn
[†] hcni@lps.ecnu.edu.cn
[‡] jwu@phy.ecnu.edu.cn

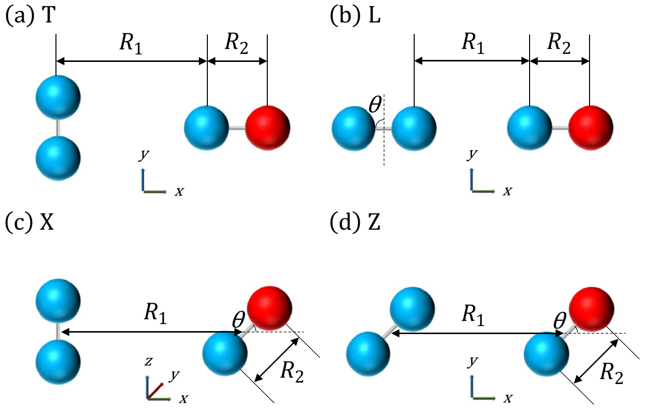

FIG. 1. Different initial configurations of the $D_2$-$D_2$ dimer.

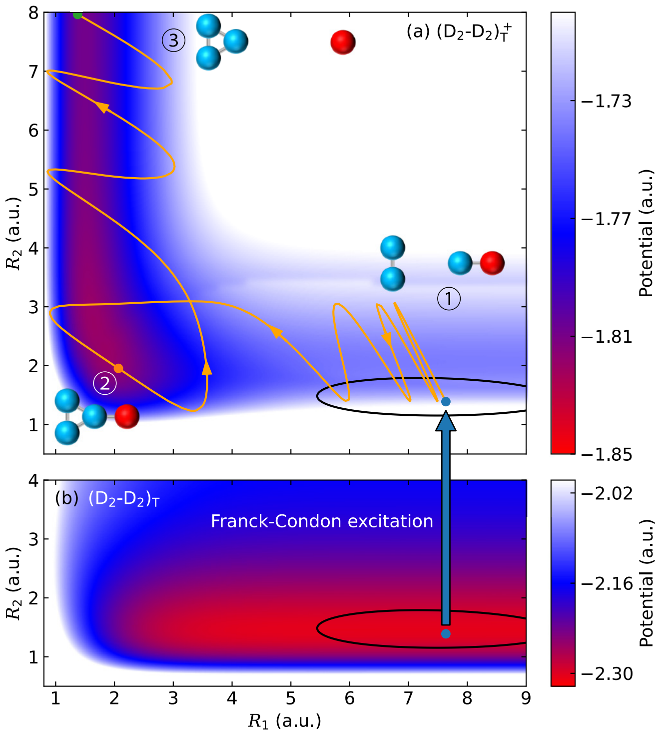

FIG. 2. Potential energy surfaces of the T-type $D_2$-$D_2$ dimer complex in both its (a) cationic and (b) neutral states, with the ground-state probability distribution highlighted by black contour lines. In panel (a), a representative reaction trajectory leading to the formation of $D_3{}^+$ is depicted by the orange curve. The dimer configurations at various points along this trajectory are displayed as insets.

ultrafast reaction dynamics starting from different initial geometric configurations of the neutral $D_2$-$D_2$ dimer. The intricate microscopic details of bimolecular reactions are important for further understanding intermolecular interactions.

The article is organized as follows. In Sec. II, we summarize the initial stable geometric configurations of the neutral $D_2$-$D_2$ dimer, elucidate the ultrafast process of the bimolecular reaction, and detail the theoretical methods for the timing of the reaction dynamics. In Sec. III, we comparatively investigate the role of quantum effects of the nuclei using a variety of theoretical methods starting from the most stable and populated initial configuration. In Sec. IV, we explore the influence of the initial nuclear momentum on the subsequent molecular dynamics. In Sec. V, we systematically study the details of ultrafast reaction dynamics starting from different initial geometric configurations. Conclusions are given in Sec. VI. Atomic units are used throughout unless stated otherwise.

## II. THEORETICAL FRAMEWORK

### A. Initial configurations

The $D_2$-$D_2$ dimer complex, comprising four atoms, can be fully characterized by a six-dimensional potential energy surface. This surface exhibits a number of local minima, each supporting a stable local geometric configuration. These stable points correspond to the initial configurations of the neutral dimer, a crucial factor enabling precise time resolution of the ensuing reaction dynamics by providing a well-defined spatial starting point.

Previous investigations have revealed several stable initial structural configurations of the neutral dimer, which encompass the T, L, X, and Z shapes [35], as visually depicted in Fig. 1. For each of these geometric configurations, we establish an approaching coordinate denoted as $R_1$ and a departing coordinate represented by $R_2$. As the reaction progresses, the approaching distance $R_1$ gradually decreases, culminating in the formation of trihydrogen, while the departing distance $R_2$ concurrently increases, leading to the departure of the remaining hydrogen atom, indicated in red. In the case of the most stable T configuration, the definition of $R_1$ and $R_2$ as the reaction coordinates is sufficient, as they are the principal coordinates directly relevant to the reaction. However, for other initial configurations, an additional rotation angle, $\theta$, must be introduced to enable the formation of the stable, triangle-shaped $D_3{}^+$.

### B. Reaction mechanism

To explore the quantum effects on reaction dynamics and gain insights into the application of different quantum methods in molecular dynamics simulations, we conduct a comparative analysis between classical and quantum methods to calculate the timescale of trihydrogen cation formation. Considering the various structural configurations of this reaction, we initiate our investigation with the most stable T-type configuration. As illustrated in Fig. 1(a), the T-type configuration features two molecular axes perpendicular to each other; this configuration has the lowest equilibrium energy and represents the most probable configuration. As shown in Fig. 2, by defining two reaction coordinates, $R_1$ and $R_2$, the PES of the cationic $(D_2\text{-}D_2)^+$ dimer and the neutral $D_2$-$D_2$ dimer are calculated using the complete-active-space self-consistent field (CASSCF) method at the CAS(3,4) and CAS(4,4) levels with the aug-cc-pVTZ basis set. The active space includes two occupied and two unoccupied orbitials and all electrons are active, which is sufficient for the calculations of the $D_2$-$D_2$ dimer. The initial equilibrium geometry of the neutral dimer is determined at $R_1 = 7.635$ a.u. and $R_2 = 1.390$ a.u.

The formation of $D_3{}^+$ can proceed via three steps, as illustrated in Fig. 2. Initially, upon Franck-Condon excitation, the cationic state populates around the equilibrium geometry of the neutral state (referred to as step ①). Under the force field of the cationic state, the nuclear dynamics follow a typical trajectory indicated by the orange curve in Fig. 2(a). Notably, as the hydrogen molecule at the right end undergoes single ionization, the $D_2{}^+$ ion begins to vibrate around the new equilibrium internuclear distance of $R_2 = 2.0$ a.u. while simultaneously approaching the neutral $D_2$ molecule at the left end. This results in an intermediate state where all four particles become adjacent (step ②). Finally, the departure of the neutral D atom at a longer time delay signifies the formation of the $D_3{}^+$ cation (step ③).

### C. Simulation methods

In this section, we provide an overview of the main computational methods employed in our study, including both classical and quantum approaches. Our benchmark begins with classical-trajectory Monte Carlo (CTMC) simulations, which are then compared to the outcomes of TDSE, BM, and BP.

#### *1. Classical-trajectory Monte Carlo*

The Born-Oppenheimer approximation separates the motion of atomic nuclei and the calculation of electron structure, streamlining the analysis of nuclear motion. CTMC, as a powerful implementation of continuum propagation, neglects quantum effects but fully accounts for molecular potential energy during nuclear motion. Setting the initial conditions of trajectories, involving both initial position and velocity, constitutes the initial crucial step in CTMC. In our simulations, the initial positions are sampled from the ground-state nuclear wave function on the neutral dimer state (depicted by black contour lines in Fig. 2). This approach naturally incorporates anharmonic effects compared to traditional methods. The ground-state nuclear wave function is derived from imaginary-time propagation by solving the TDSE, as elaborated below.

Once the initial conditions are set, the trajectories are evolved according to the Newtonian equation of motion:

$$m\ddot{\boldsymbol{r}} = -\nabla V(\boldsymbol{r}), \tag{1}$$

where $V(\boldsymbol{r})$ represents the PES of the cationic $(D_2\text{-}D_2)^+$ dimer and $m$ is the generalized mass, which depends on the specific configuration and coordinate system where it is defined. Within the $R_1$-$R_2$ coordinate system of the T-type configuration as in Fig. 1(a), $m$ can be written as

$$m = \begin{bmatrix} m_D & m_D/2 \\ m_D/2 & 3m_D/4 \end{bmatrix}, \tag{2}$$

where $m_D$ is the mass of the D atom. To ensure sufficient statistical accuracy, a swarm of 10 000 nuclear trajectories is evolved on the PES with zero initial velocity. Once all trajectories have completed their propagation, we extract time-related information. We consider $D_3{}^+$ formed when the approaching distance $R_1$ is smaller than 4 a.u. and the departing distance $R_2$ is larger than 5 a.u. Subsequently, trajectories leading to the formation of $D_3{}^+$ are collected, allowing us to construct a histogram of the formation time of these trajectories for detailed analysis of the reaction timescale.

#### *2. Time-dependent Schrödinger equation*

As a well-developed quantum theory, TDSE offers a comprehensive quantum perspective for studying molecular dynamics. In the current work, the TDSE is solved within the framework of nonrelativistic quantum mechanics to describe the motion of the nuclear wave packet governed by

$$i\frac{\partial}{\partial t}\psi(\boldsymbol{r},t) = \left[\frac{\boldsymbol{p}^2}{2m} + V(\boldsymbol{r})\right]\psi(\boldsymbol{r},t). \tag{3}$$

The TDSE is propagated using the split-operator Fourier method. The initial nuclear wave function is obtained as the ground state of the neutral dimer, which is calculated through imaginary-time propagation by setting $V(\boldsymbol{r})$ as the PES of the neutral state.

Following Franck-Condon excitation, the nuclear wave function undergoes quantum dynamical evolution on the PES of the cationic state. To this end, we populate the initial nuclear wave function on the PES of the cationic $(D_2\text{-}D_2)^+$ dimer and allow the nuclear wave function to evolve freely.

The PES of the T-type $D_2$-$D_2$ dimer has been calculated within the scope of $0.5 < R_1 < 13.8$ and $0.5 < R_2 < 10.5$, covering the essential region where molecular dynamics occurs, and the time evolution of the nuclear wave function has been correspondingly carried out within this range. We have used a time step of $\Delta t = 1$ and a spatial step of $\Delta R_1 = \Delta R_2 = 0.013$, and convergence has been achieved with this grid parameter. Meanwhile, an absorption boundary is employed to prevent reflection of the nuclear wave packet from the grid border.

In order to extract the time-related information of this reaction, we employ the virtual detector method [19–22] to obtain the probability flux of the wave function at the position defining the formation of $D_3{}^+$: $R_1 < 4$ a.u. and $R_2 = 5$ a.u. where the virtual detectors are placed right on the grid points. The probability flux at the position $\boldsymbol{r}_d$ of a specific virtual detector can be calculated as

$$\boldsymbol{j}(\boldsymbol{r}_d,t) = -\frac{i}{2m}[\psi^*(\boldsymbol{r}_d,t)\nabla\psi(\boldsymbol{r}_d,t) - \text{c.c.}]. \tag{4}$$

Upon accumulating all detector signals, the distribution of the probability flux (projected onto the direction of the departing coordinate $R_2$) over time can be analyzed to determine the reaction time of the formation process.

#### *3. Bohmian mechanics*

Originally proposed by Louis de Broglie and later elaborated upon by David Bohm, BM serves as a complementary yet fully equivalent quantum approach to the TDSE, describing quantum evolution in terms of trajectorylike language [30]. In this approach, the nuclear wave function can be expressed in polar form as

$$\psi(\boldsymbol{r},t) = R(\boldsymbol{r},t)e^{iS(\boldsymbol{r},t)}, \tag{5}$$

where $R(\boldsymbol{r},t)$ represents the amplitude and $S(\boldsymbol{r},t)$ denotes the phase of the nuclear wave function. Inserting this polar form [Eq. (5)] into the TDSE [Eq. (3)] results in two coupled differential equations:

$$\frac{\partial S}{\partial t}+\frac{(\nabla S)^2}{2m}+V(\boldsymbol{r})+Q(\boldsymbol{r},t)=0, \tag{6}$$

$$\frac{\partial \rho}{\partial t}+\nabla\cdot\left(\frac{\rho \boldsymbol{p}}{m}\right)=0, \tag{7}$$

where $\rho(\boldsymbol{r},t)=R^2(\boldsymbol{r},t)=|\psi(\boldsymbol{r},t)|^2$ is the probability density and $\boldsymbol{p}=\nabla S(\boldsymbol{r},t)$ is the momentum of the nucleus. Equation (7) is the continuity equation, while Eq. (6) is referred to as the quantum Hamilton-Jacobi equation in BM.

Notably, in comparison to the classical Hamilton-Jacobi equation, Eq. (6) incorporates an additional term:

$$Q(\boldsymbol{r},t)=-\frac{1}{2}\frac{\nabla^2 R(\boldsymbol{r},t)}{R(\boldsymbol{r},t)}, \tag{8}$$

known as the quantum potential in BM. This term introduces nonlocality, thereby incorporating quantum features distinct from classical trajectories.

Based on Eqs. (6) and (7), a Bohm-Newton equation of motion can be derived:

$$m\ddot{\boldsymbol{r}}=-\nabla[V(\boldsymbol{r})+Q(\boldsymbol{r},t)], \tag{9}$$

whose direct solution is, however, difficult. Instead, one usually resort to a much simpler equation of motion:

$$m\dot{\boldsymbol{r}}=\nabla S(\boldsymbol{r},t), \tag{10}$$

where $S(\boldsymbol{r},t)=\arg\psi(\boldsymbol{r},t)$ is the time-dependent phase of the wave function obtained by solving the TDSE. Therefore, the Bohmian trajectories are guided by the pilot wave $\psi(\boldsymbol{r},t)$ calculated by the TDSE. Finally, similar to the case of CTMC, time-related information can be extracted using this approach.

#### *4. Backpropagation*

The backpropagation method [31–34] involves a full quantum propagation of the nuclear wave function forward in time, followed by a classical backpropagation of the target portion of the wave function to pinpoint the formation time of $D_3{}^+$. During the forward phase, akin to the TDSE method, virtual detectors are positioned at $R_1 < 4$ a.u. and $R_2 = 7$ a.u., where all quantum flux is outward, representing the eventual formation of $D_3{}^+$. This portion of the wave function is then transformed into classical trajectories and propagated backward in time to extract their temporal information. The local momentum required to initiate backpropagation is computed by substituting Eq. (5) into Eq. (4):

$$\boldsymbol{p}(\boldsymbol{r}_d,t)\equiv\nabla S(\boldsymbol{r}_d,t)=\frac{m\boldsymbol{j}(\boldsymbol{r}_d,t)}{\rho(\boldsymbol{r}_d,t)}. \tag{11}$$

Subsequently, the resulting phase-space density $\rho(\boldsymbol{r},t)$ is propagated backward in time with classical trajectories $[\boldsymbol{p}(t),\boldsymbol{r}(t)]$ until $R_2 = 5$ a.u. The resulting distribution of the formation times of $D_3{}^+$ is then compiled.

## III. ULTRAFAST REACTION DYNAMICS

To investigate quantum effects in chemical reactions and molecular dynamics, we present in Fig. 3 the normalized distribution of the formation rate of $D_3{}^+$ starting from the T-type initial configuration of the neutral dimer, calculated by different theoretical methods: CTMC [panel (a)], BM [panel (b)], TDSE [panel (c)], and BP [panel (d)]. While CTMC is a purely classical method, BM and TDSE are purely quantum methods, and BP is a hybrid quantum-classical method. The distributions of the formation time obtained from these methods are subsequently fitted with the Gamma distribution given by

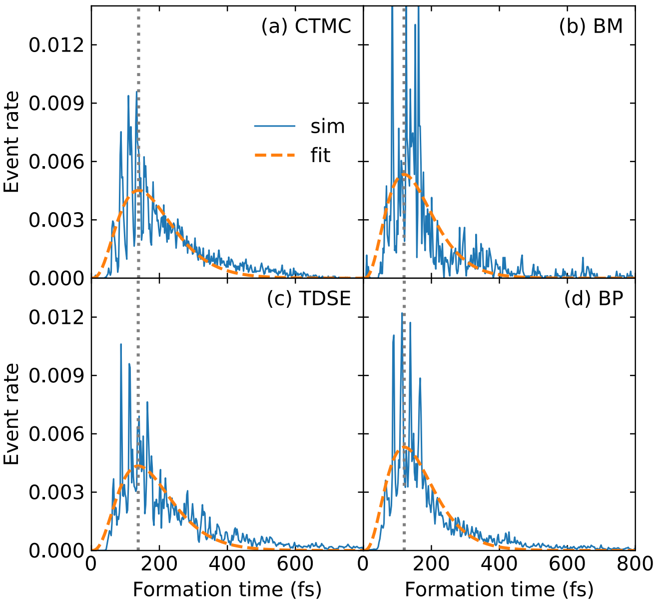

FIG. 3. Histogram of the $D_3{}^+$ formation time calculated by (a) classical-trajectory Monte Carlo (CTMC), (b) Bohmian trajectory (BM), (c) time-dependent Schrödinger equation (TDSE), and (d) backpropagation (BP) methods.

$$f(t)=\alpha t^{k-1}e^{-t/\tau}, \tag{12}$$

which is frequently used to model time distributions in Poisson processes, where $\alpha$ is an overall scaling factor, $k = 4$ is the shape parameter for the T-type configuration, and $\tau$ is the scale parameter. The gray dotted lines in each panel in Fig. 3 indicate the peak position of the fitted curves, representing the peak reaction time.

In Fig. 3, the peak formation time obtained using CTMC is 138.8 fs, while the peak formation time is 119.2 fs as obtained from BM. Comparing Eqs. (1) and (9), we note that the difference between the two equations lies in the presence of the quantum potential $Q(\boldsymbol{r},t)$. Therefore, the small disparity in the reaction time calculated by CTMC and BM methods can be attributed to the quantum effects introduced by the quantum potential $Q(\boldsymbol{r},t)$.

Results from both BM and TDSE methods are based on the quantum wave function. Compared to BM, the formation time extracted from TDSE is a little longer, at 137.7 fs. As mentioned earlier, the $D_2{}^+$ ion approaches the $D_2$ molecule while vibrating around the new equilibrium internuclear distance. Until $D_3{}^+$ is formed with the departure of the neutral D atom, an oscillation in the distance between the nuclei of the $D_2{}^+$ ion persists, implying that, at certain time instances, the distance $R_2$ may get close to or even exceed 5 a.u. during the oscillation before the formation of $D_3{}^+$. Leveraging the trajectorylike language in the BM method allows us to directly determine the formation time by observing the last

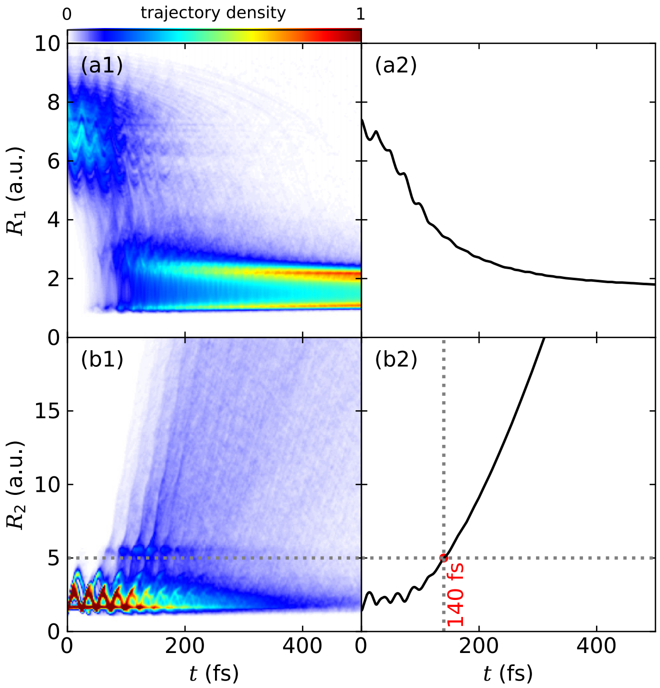

FIG. 4. Ultrafast reaction dynamics of the T-shape configuration. Column (1) displays the classical trajectories leading to the formation of $D_3^+$. Column (2) indicates the average value of these trajectories on the $R_1$ and $R_2$ coordinates at each moment.

instance when Bohmian trajectories cross the $R_2 = 5$ a.u. boundary. In contrast, in TDSE, wave packets approaching $R_2 = 5$ a.u. before the formation of $D_3^+$ are indiscriminately detected by virtual detectors, leading to additional signals and consequently distinct peak formation times compared to the BM method.

BP provides an alternative solution to this issue. The BP method comprises two stages: forward evolution of the nuclear wave packet and the backpropagation of classical trajectories. The forward evolution aligns with the TDSE method, with the only difference being the placement of virtual detectors further away to ensure the complete formation of $D_3^+$. Consequently, the corresponding reaction has already concluded before detection, significantly reducing interference between the signals. When the virtual detectors located at $R_2 = 7$ a.u. detect a signal, it is converted into a classical trajectory and backpropagated. The first instance when the particle reverses its path and reaches $R_2 = 5$ a.u. is considered the $D_3^+$ formation time of this trajectory. Using this approach, the reaction time obtained by the BP method is determined to be 120.1 fs, very close to the results from BM. This demonstrates the existence of quantum effects, albeit small, on the motion of atomic nuclei.

Considering the significantly longer computation times of BM and BP methods compared to TDSE, TDSE remains a reasonable choice for quantum computations within an acceptable margin of error. For highly accurate studies of quantum effects, however, BM and BP methods offer superior precision.

The distributions of formation rates obtained from all methods exhibit a common feature: multiple peaks can be observed in the early stage of the histogram. This observation could be hypothesized to be related to the vibration of $D_2^+$ upon photoionization of $D_2$ [36]. To substantiate this conjecture, the classical trajectories leading to the formation of $D_3^+$ are plotted in Figs. 4(a1) and 4(b1). As depicted in Fig. 4(b1), $D_2^+$, formed via single ionization of $D_2$, vibrates while approaching $D_2$. Whenever the average internuclear distance of $D_2^+$ reaches a local maximum, the probability of its dissociation to form $D_3^+$ also peaks subsequently. Combining this observation with the PES in Fig. 2(a), one may conclude that, as $R_1$ decreases, the neutral $D_2$ molecule depresses the PES of $D_2^+$, leading to dissociation. Hence, when $R_2$ vibrates to a maximal value, $R_1$ of the complex simultaneously reaches a minimal value, resulting in a relatively high probability of $D_3^+$ formation.

Figures 4(a2) and 4(b2) display the average values of the trajectories on the $R_1$ and $R_2$ coordinates at each moment, reflecting the average reaction process in the T-shape configuration. The intersection of the two dashed gray lines in Fig. 4(b2) indicates the average time of $D_3^+$ formation, which is very close to the formation time calculated by the CTMC method. Consequently, analyzing the internal nuclear motion of the reaction can be achieved by tracking the average positions of the trajectories over time.

## IV. INFLUENCE OF INITIAL NUCLEAR MOMENTUM

Up to now, we have assumed the initial momentum of the nuclear trajectory to be zero. We proceed to explore the possible influence of a distribution of initial nuclear momentum on the subsequent molecular dynamics. From the neutral ground state of the nuclear wave function $\psi_0(R_1, R_2)$, in principle, a four-dimensional Wigner quasiprobability distribution $\rho_0(R_1, P_1, R_2, P_2)$ needs to be constructed, where $P_1$ and $P_2$ are the conjugate momenta of $R_1$ and $R_2$, respectively. This four-dimensional distribution is heavy to construct. However, the procedure can be simplified if one considers the dimensions of $R_1$ and $R_2$ to be independent of each other, or $\psi_0(R_1, R_2) = \psi_0(R_1) \otimes \psi(R_2)$, where $\psi_0(R_1) = \psi_0(R_1, R_2 = R_2^{(0)})$ is assessed at the equilibrium position of $R_2$ and $\psi_0(R_2) = \psi_0(R_1 = R_1^{(0)}, R_2)$ is assessed at the equilibrium position of $R_1$. This can be justified by the fact that the dynamics in $R_1$ and $R_2$ are largely decoupled, which can be seen also from the contour plot of the initial-state distribution in Fig. 2, whose symmetric shape indicates it is roughly a direct product of the individual distributions in $R_1$ and $R_2$. Thereby, the Wigner quasiprobability distribution can be approximated by $\rho_0(R_1, P_1, R_2, P_2) = \rho_0(R_1, P_1) \otimes \rho_0(R_2, P_2)$, where $\rho_0(R_i, P_i)$ is the individual quasiprobability distribution for coordinate $R_i$.

Shown in Figs. 5(a) and 5(b) are the Wigner quasiprobability distributions of $\rho_0(R_1, P_1)$ and $\rho_0(R_2, P_2)$, respectively. Clearly, the initial momentum is no longer simply zero. Rather, the trajectories are now sampled according to the quasiprobability distribution. With this Wigner sampling, we carry out CTMC simulations and extract the formation time distribution as shown in Fig. 5(c). Through fitting, the most probable reaction time is determined to be 136.4 fs, close to that obtained by CTMC simulations with zero initial velocity. It is thus clear that the initial distribution of nuclear

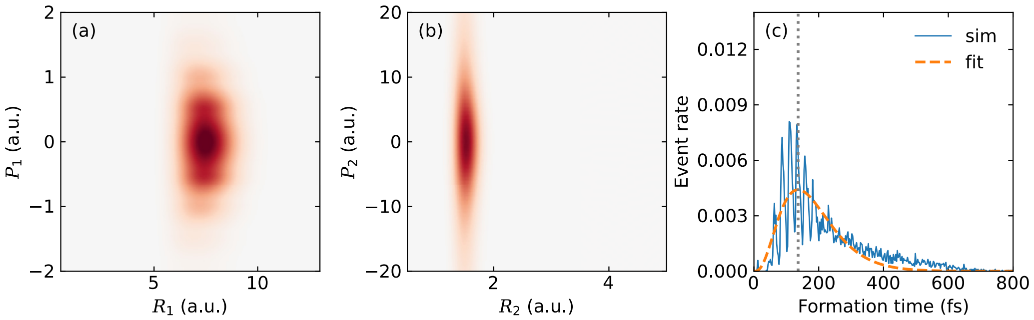

FIG. 5. Wigner quasiprobability distribution (a) $\rho_0(R_1, P_1)$ and (b) $\rho_0(R_2, P_2)$, and (c) the formation time distribution using CTMC with Wigner sampling.

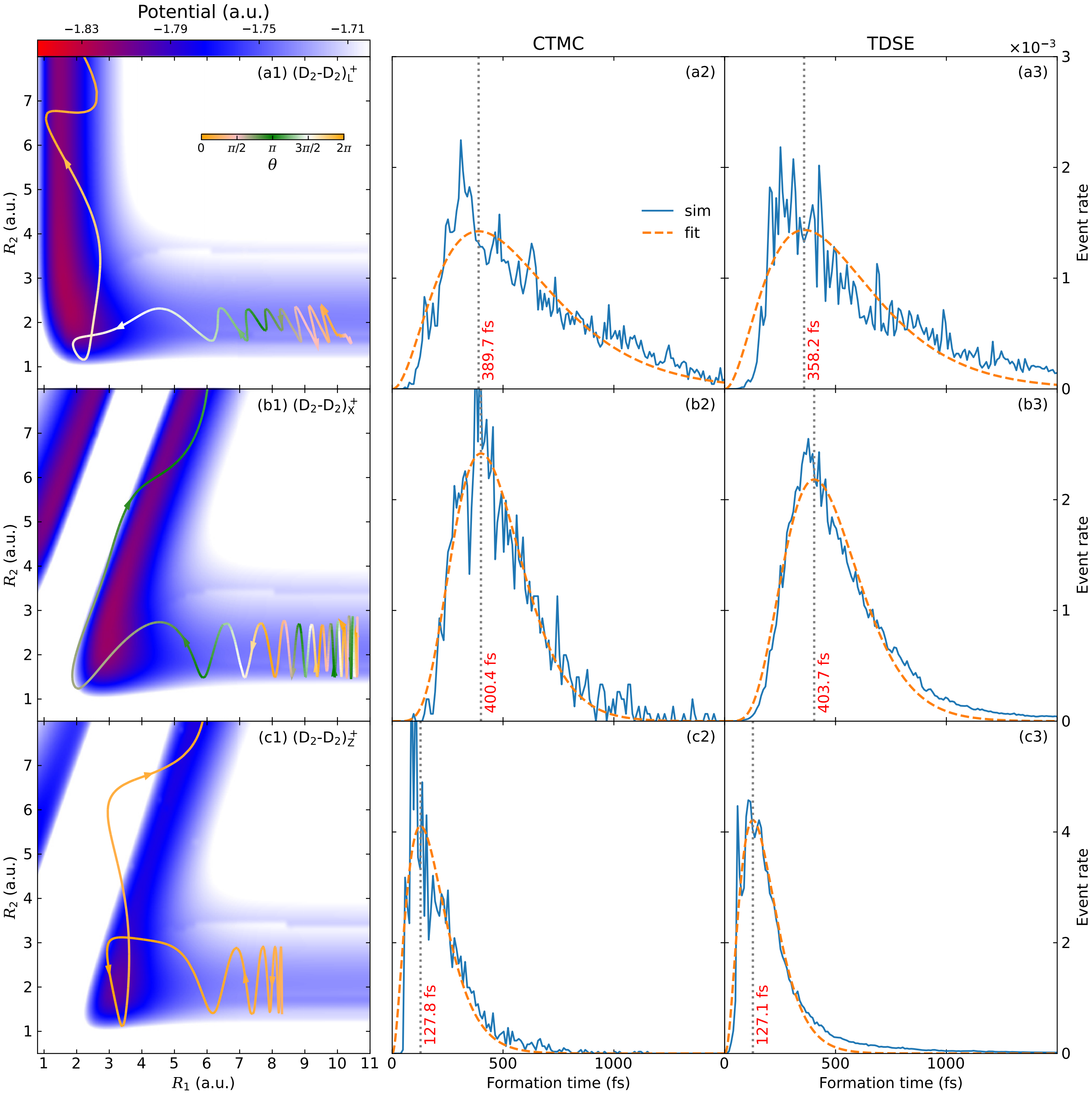

FIG. 6. Results starting from different initial configurations, including L-type [row (a)], X-type [row (b)], and Z-type [row (c)]. Column 1: PES of cationic $(D_2\text{-}D_2)^+$ at $\theta = 0$. Column 2: Histogram of the formation time calculated by CTMC. Column 3: Histogram of the formation time calculated by TDSE.

momentum has only minor influences on the subsequent molecular dynamics.

## V. DIFFERENT INITIAL CONFIGURATIONS

In this section, we carry out a systematic exploration of the chemical reaction starting from various initial geometric configurations of the neutral dimer. For the sake of simplicity, we perform only CTMC and TDSE calculations for the L, X, and Z configurations, besides the T configuration discussed above. The PES at $\theta = 0$ and the corresponding histogram of the formation time for different configurations are presented in Fig. 6.

In the X and Z shapes, the definition of $R_1$ is the distance between the center of mass of $D_2$ and $D_2^+$, which differs from that of the T and L shapes. A trajectory in X or Z shapes leading to the formation of $D_3^+$ exhibits a slope close to 2 in the $R_1$-$R_2$ plane. Fitting the data to the Gamma distribution [Eq. (12)], we can obtain the peak reaction times for different initial configurations, as marked by the dashed gray lines.

As evident from Fig. 6, the calculated results are heavily dependent on the initial geometric configuration. The reaction times in L and X shapes are longer than those in T and Z shapes partially due to the larger equilibrium distance between two reactants in L and X shapes. Another important reason is the rotation of the molecule for L and X types (discussed below). Consequently, it takes more time for the two molecules to come together and react, forming $D_3^+$.

In shapes other than T, rotation of the molecule is necessary to form $D_3^+$, complicating the dynamics of the trajectories. To demonstrate the rotation dynamics, we use the color code to indicate the variation in the angular coordinate $\theta$ as the reaction progresses, as shown in Figs. 6(a1), 6(b1), and 6(c1). For L and X configurations, the molecule may rotate for a few rounds before $D_3^+$ could be possibly formed, leading to long formation times. In contrast, a rotation in the angle $\theta$ is not a must for the Z configuration, as demonstrated by the near uniform color of the typical trajectory in Fig. 6(c1). Thereby, the peak formation time is short for the Z configuration.

When both vibration and rotation are considered simultaneously, the multiple peaks in the time distribution, as observed in the T shape, become less distinct. This occurs because only when the rotation of the molecule reaches an appropriate dissociation angle can the dimer react to form $D_3^+$. However, $R_2$ is not necessarily at a local maximum during this process, which makes it difficult to manifest the vibration of $D_2^+$ and significantly reduces the yield in L, X, and Z shapes.

The initial positions of the classical trajectories are sampled based on the ground-state nuclear wave function of the neutral dimer, inherently considering anharmonic effects to avoid the generation of nonphysical fast trajectories. This approach ensures the accuracy of the present calculations, leading to longer reaction times in all configurations compared to those reported in previous studies [17].

Notably, the formation times calculated by both CTMC and TDSE methods are comparable across all configurations, demonstrating the general applicability of both classical and quantum methods in the bimolecular reaction. Despite the disturbance induced by interference, our calculations pave the way for integrating quantum methods into the studies of nuclear dynamics during chemical reactions.

## VI. CONCLUSION

In summary, we have investigated the ultrafast bimolecular reaction of the $D_2$-$D_2$ dimer upon photoionization, leading to the formation of $D_3^+$. By exploring various initial geometric configurations (T, L, X, and Z shapes), we have provided a comprehensive understanding of nuclear motion from both classical and quantum perspectives. Several theoretical methods, including classical trajectory Monte Carlo, time-dependent Schrödinger equation, Bohmian mechanics, and the backpropagation method, were employed to dissect the reaction dynamics. By defining primary reaction coordinates, the potential energy surface was constructed for detailed analysis of the relevant reaction dynamics. We compared classical and quantum methods, affirming the reliability of these techniques. Notably, the quantum effects play an overall minor role in the reaction time. Our study further extends beyond the T configuration, venturing into the L, X, and Z shapes, providing a holistic view of the reaction dynamics. This systematic approach uncovers configuration-dependent reaction dynamics, demonstrating the important impact of geometric variations on reaction times. Anharmonic effects, essential in avoiding nonphysical trajectories, were inherently considered, ensuring the accuracy of the results. Our study on ultrafast bimolecular reactions not only enhances our understanding of detailed molecular dynamics but also lays the foundation for future studies, promising deeper insights into intricate quantum processes guiding chemical reactions.

## ACKNOWLEDGMENTS

This work is supported by the National Natural Science Foundation of China (Grants No. 92150105, No. 22173017, No. 12227807, and No. 12241407) and the Science and Technology Commission of Shanghai Municipality (Grants No. 21ZR1420100, No. 22511103900, and No. 23JC1402000). Numerical computations were in part performed on the East China Normal University Multifunctional Platform for Innovation (001).

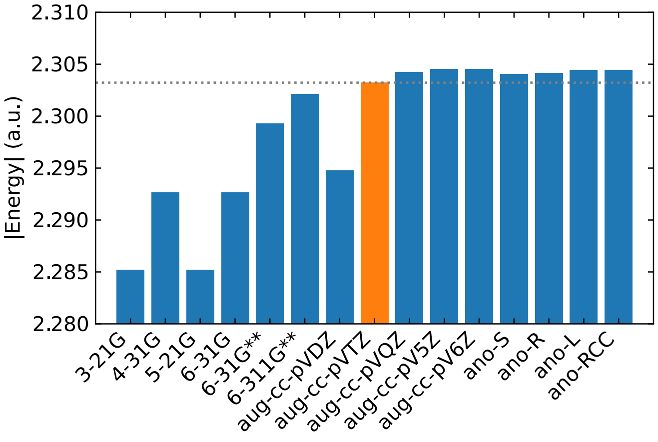

FIG. 7. The potential energy of the T-type $D_2$-$D_2$ dimer at $R_1 = 7.131$ a.u. and $R_2 = 1.427$ a.u. using different basis sets.

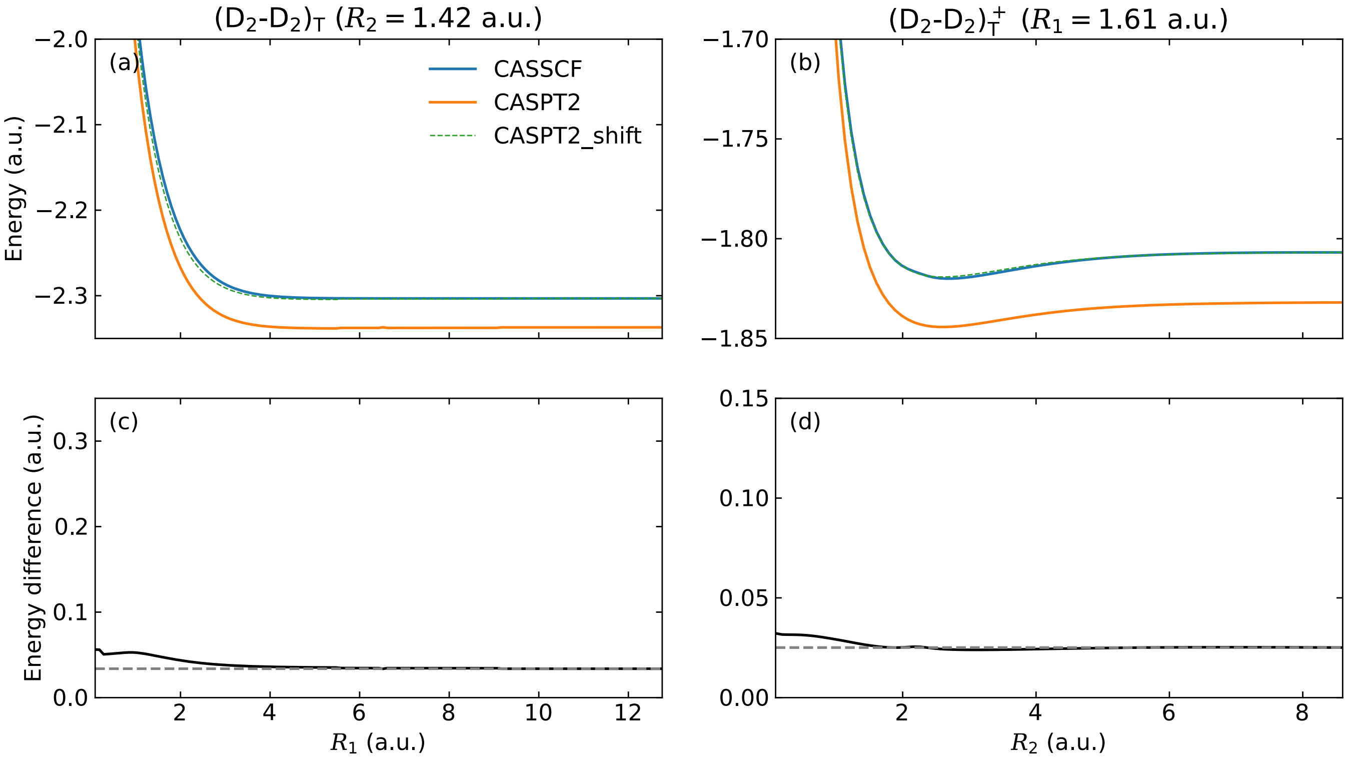

FIG. 8. The PES of the (a) neutral $(D_2\text{-}D_2)_T$ dimer at $R_2 = 1.42$ a.u. and (b) cationic $(D_2\text{-}D_2)_T{}^+$ dimer at $R_1 = 1.61$ a.u. calculated by CASSCF and CASPT2 methods. The black solid curves in panels (c) and (d) are the corresponding difference between the potential energy curves obtained by the two methods in panels (a) and (b).

## APPENDIX: ACCURACY OF THE POTENTIAL ENERGY SURFACE

An accurate PES is important for the computation of the molecular dynamics. To check the accuracy of our calculations, we have performed the potential energy calculations of the neutral dimer in the T configuration at $R_1 = 7.131$ a.u. and $R_2 = 1.427$ a.u. using various basis sets, as shown in Fig. 7. It is clear that aug-cc-pVTZ is sufficient for the accuracy. Considering the calculation time, the aug-cc-pVTZ basis set is an ideal choice that balances speed and accuracy.

In addition, the PES is calculated using the CASSCF method. We have compared it with the more accurate method of complete-active-space second-order perturbation theory (CASPT2) in Fig. 8. Figure 8(a) is the calculated PES of the neutral $(D_2\text{-}D_2)_T$ dimer at $R_2 = 1.42$ a.u. and Fig. 8(b) is that of the cationic $(D_2\text{-}D_2)_T{}^+$ dimer at $R_1 = 1.61$ a.u. Figures 8(c) and 8(d) are the corresponding difference in energy obtained by different theoretical methods. It is clear that CASPT2 gives an overall lower energy than CASSCF. The difference in energy is, however, a largely constant value. It is important to note that it is the spatial gradient of the potential, namely force, that governs the nuclear motion, as shown in Eq. (1). Thus, the overall shift in the potential energy is not important. Although the energy difference is not flat for very small $R_1$ and $R_2$ coordinates, the gradient in the potential itself is very large there, leading to strong repulsions, and the trajectories can hardly reach these regions. Hence, using the CASSCF PES only leads to minor difference from using the CASPT2 PES. Therefore, we have chosen CASSCF, which is computationally much less heavy, for the calculation of the PES.

---

[1] J. Tennyson, Spectroscopy of $H_3{}^+$: planets, chaos and the universe, Rep. Prog. Phys. **58**, 421 (1995).

[2] J. H. D. Eland, The origin of primary $H_3{}^+$ ions in mass spectra, Rapid Commun. Mass Spectrom. **10**, 1560 (1996).

[3] B. J. McCall and T. Oka, $H_3{}^+$—an ion with many talents, Science **287**, 1941 (2000).

[4] T. R. Geballe and T. Oka, A key molecular ion in the universe and in the laboratory, Science **312**, 1610 (2006).

[5] T. Oka, Interstellar $H_3{}^+$, Proc. Natl. Acad. Sci. USA **103**, 12235 (2006).

[6] K. Hoshina, Y. Furukawa, T. Okino, and K. Yamanouchi, Efficient ejection of $H_3{}^+$ from hydrocarbon molecules induced by ultrashort intense laser fields, J. Chem. Phys. **129**, 104302 (2008).

[7] P. M. Kraus, M. C. Schwarzer, N. Schirmel, G. Urbasch, G. Frenking, and K.-M. Weitzel, Unusual mechanism for $H_3{}^+$ formation from ethane as obtained by femtosecond laser pulse ionization and quantum chemical calculations, J. Chem. Phys. **134**, 114302 (2011).

[8] T. Oka, Interstellar $H_3{}^+$, Chem. Rev. **113**, 8738 (2013).

[9] N. Ekanayake, M. Nairat, B. Kaderiya, P. Feizollah, B. Jochim, T. Severt, B. Berry, K. R. Pandiri, K. D. Carnes, S. Pathak *et al.*, Mechanisms and time-resolved dynamics for trihydrogen cation ($H_3^+$) formation from organic molecules in strong laser fields, Sci. Rep. **7**, 4703 (2017).

[10] N. Ekanayake, T. Severt, M. Nairat, N. P. Weingartz, B. M. Farris, B. Kaderiya, P. Feizollah, B. Jochim, F. Ziaee, K. Borne *et al.*, $H_2$ roaming chemistry and the formation of $H_3^+$ from organic molecules in strong laser fields, Nat. Commun. **9**, 5186 (2018).

[11] S. Miller, J. Tennyson, T. R. Geballe, and T. Stallard, Thirty years of $H_3^+$ astronomy, Rev. Mod. Phys. **92**, 035003 (2020).

[12] M. S. Alghabra, R. Ali, V. Kim, M. Iqbal, P. Rosenberger, S. Mitra, R. Dagar, P. Rupp, B. Bergues, D. Mathur *et al.*, Anomalous formation of trihydrogen cations from water on nanoparticles, Nat. Commun. **12**, 3839 (2021).

[13] T. R. Hogness and E. G. Lunn, The ionization of nitrogen by electron impact as interpreted by positive ray analysis, Phys. Rev. **26**, 786 (1925).

[14] L. Doverspike and R. L. Champion, Experimental investigations of ion–molecule reactions of $D_2^+$ with $D_2$ and $H_2$, J. Chem. Phys. **46**, 4718 (1967).

[15] J. Krenos, K. Lehmann, J. Tully, P. Hierl, and G. Smith, Crossed-beam study of the reactions of $H_2^+$ with $D_2$ and $D_2^+$ with $H_2$, Chem. Phys. **16**, 109 (1976).

[16] J. Pollard, D. Lichtin, and R. Cohen, Differential cross sections for state-selected reactions in the $H_2^+ + H_2$ system, Chem. Phys. Lett. **152**, 171 (1988).

[17] L. Zhou, H. Ni, Z. Jiang, J. Qiang, W. Jiang, W. Zhang, P. Lu, J. Wen, K. Lin, M. Zhu, R. Dörner, and J. Wu, Ultrafast formation dynamics of $D_3^+$ from the light-driven bimolecular reaction of the $D_2$-$D_2$ dimer, Nat. Chem. **15**, 1229 (2023).

[18] Y. Mi, E. Wang, Z. Dube, T. Wang, A. Naumov, D. Villeneuve, P. Corkum, and A. Staudte, $D_3^+$ formation through photoionization of the molecular $D_2$-$D_2$ dimer, Nat. Chem. **15**, 1224 (2023).

[19] B. Feuerstein and U. Thumm, On the computation of momentum distributions within wavepacket propagation calculations, J. Phys. B **36**, 707 (2003).

[20] X. Wang, J. Tian, and J. H. Eberly, Extended virtual detector theory for strong-field atomic ionization, Phys. Rev. Lett. **110**, 243001 (2013).

[21] X. Wang, J. Tian, and J. Eberly, Virtual detector theory for strong-field atomic ionization, J. Phys. B **51**, 084002 (2018).

[22] R.-H. Xu and X. Wang, Extended virtual detector theory including quantum interferences, AIP Adv. **11**, 025124 (2021).

[23] D. Bohm, A suggested interpretation of the quantum theory in terms of “hidden” variables. I, Phys. Rev. **85**, 166 (1952).

[24] D. Bohm, A suggested interpretation of the quantum theory in terms of “hidden” variables. II, Phys. Rev. **85**, 180 (1952).

[25] C. L. Lopreore and R. E. Wyatt, Quantum wave packet dynamics with trajectories, Phys. Rev. Lett. **82**, 5190 (1999).

[26] X. Lai, Q.-Y. Cai, and M. Zhan, From a quantum to a classical description of intense laser–atom physics with Bohmian trajectories, New J. Phys. **11**, 113035 (2009).

[27] G. Albareda, D. Marian, A. Benali, S. Yaro, N. Zanghì, and X. Oriols, Time-resolved electron transport with quantum trajectories, J. Comput. Electron. **12**, 405 (2013).

[28] A. Benseny, G. Albareda, Á. S. Sanz, J. Mompart, and X. Oriols, Applied Bohmian mechanics, Eur. Phys. J. D **68**, 286 (2014).

[29] T. A. Elsayed, K. Mølmer, and L. B. Madsen, Entangled quantum dynamics of many-body systems using Bohmian trajectories, Sci. Rep. **8**, 12704 (2018).

[30] X. Lai and X. Liu, Bohmian trajectory perspective on strong field atomic processes, Chin. Phys. B **29**, 013205 (2020).

[31] H. Ni, U. Saalmann, and J.-M. Rost, Tunneling ionization time resolved by backpropagation, Phys. Rev. Lett. **117**, 023002 (2016).

[32] H. Ni, U. Saalmann, and J.-M. Rost, Tunneling exit characteristics from classical backpropagation of an ionized electron wave packet, Phys. Rev. A **97**, 013426 (2018).

[33] H. Ni, N. Eicke, C. Ruiz, J. Cai, F. Oppermann, N. I. Shvetsov-Shilovski, and L.-W. Pi, Tunneling criteria and a nonadiabatic term for strong-field ionization, Phys. Rev. A **98**, 013411 (2018).

[34] Y. Ma, H. Ni, and J. Wu, Attosecond ionization time delays in strong-field physics, Chin. Phys. B **33**, 013201 (2024).

[35] A. Khan, T. Jahnke, S. Zeller, F. Trinter, M. Schöffler, L. P. H. Schmidt, R. Dörner, and M. Kunitski, Visualizing the geometry of hydrogen dimers, J. Phys. Chem. Lett. **11**, 2457 (2020).

[36] Y. Ozeki, Molecular vibrational imaging by stimulated Raman scattering microscopy: principles and applications, Chin. Opt. Lett. **18**, 121702 (2020).